

Efficient treatment of the high-frequency tail of the self-energy function and its relevance for multiorbital models

Gang Li^{1,*} and Werner Hanke¹

¹*Institut für Theoretische Physik und Astrophysik,
Universität Würzburg, 97074 Würzburg, Germany*

In this paper, we present an efficient and stable method to determine the one-particle Green's function in the hybridization-expansion continuous-time (CT-HYB) quantum Monte Carlo method, within the framework of the dynamical mean-field theory (DMFT). The high-frequency tail of the impurity self-energy is replaced with a noise-free function determined by a dual-expansion around the atomic limit. This method does not depend on the explicit form of the interaction term. More advantageous, it does not introduce any additional numerical cost to the CT-HYB simulation. We discuss the symmetries of the two-particle vertex, which can be used to optimize the simulation of the four-point correlation functions in the CT-HYB. Here, we adopt it to accelerate the dual-expansion calculation, which turns out to be especially suitable for the study of material systems with complicated band structures. As an application, a two-orbital Anderson impurity model with a general on-site interaction form is studied. The phase diagram is extracted as a function of the Coulomb interactions for two different Hund's coupling strengths. In the presence of the hybridization between different orbitals, for smaller interaction strengths, this model shows a transition from metal to band-insulator. Increasing the interaction strengths, this transition is replaced by a crossover from Mott-insulator to band-insulator behavior.

PACS numbers: 71.10.Fd, 71.27.+a, 71.30.+h

I. INTRODUCTION

The study of electronic structure of transition metal and heavy-fermion materials is one of the most active fields in condensed-matter physics. The highly correlated d - and f -electrons cannot be fully described by effective single-particle methods, such as the local-density approximation (LDA) to the density-functional theory (DFT). Here, the dynamical mean-field theory (DMFT) can be a powerful tool, especially when the momentum dependence of the self-energy is essentially negligible, regardless of the electron-electron interaction strength.¹⁻³

The central problem of the DMFT is to solve an effective impurity model. In real materials, such a model usually contains both inter- and intra-orbital interactions, as well as the hybridization among different orbitals. They account for the competitions between the magnetic, charge, and orbital fluctuations. Thus, an efficient impurity solver, which can handle all the interactions and hybridizations, is of obvious importance. Among the available impurity solvers,⁴⁻⁸ the numerically exact quantum Monte Carlo (QMC) methods were widely used. The recent development of the continuous-time quantum Monte Carlo (CT-QMC) methods⁹⁻¹² further supports the DMFT for the study of realistic materials in the sense that lower temperature regions can be reached and more orbitals can be investigated.

For realistic material calculations based on the CT-QMC solvers, correctly resolving the high-frequency behavior of the impurity self-energy $\Sigma_{imp}(i\omega_n)$ is of crucial importance. On the one hand, due to the iterative nature of the DMFT equations, $\Sigma_{imp}(i\omega_m)$ determines the Weiss function at each iteration and, in the end, the converged solution of the DMFT procedure in some cases.

On the other hand, $\Sigma_{imp}(i\omega_n)$ strongly influences the determination of the total particle number and the analytical continuation for a full spectral function calculation, which has a direct connection to experiments.

In this paper, we show how to determine the impurity self-energy for a rather general multiorbital model in an efficient and stable manner within the hybridization-expansion continuous-time (CT-HYB) method. The direct simulation in the Matsubara-frequency space and careful treatment of the self-energy high-frequency tail make this method especially suitable for studying the material systems with complex band structures.

This paper is organized as follow: Sec. II explains how the “dual transformation” can be employed to simulate effectively the one-particle Green's function in the CT-HYB. Additionally, it is shown how the simulation of the two-particle Green's function χ can be straightforwardly carried out as Wick's theorem still holds. The symmetry of χ is discussed in detail in this section. In Sec. III, we make use of the CT-HYB to study a two-orbital Hubbard model with a general interaction term. For readers who are especially interested in our CT-HYB implementation and the self-energy correction scheme, Sec. II is the primary option. If the phase diagram of the two-orbital model is of primary interest, one may skip Sec. II and go to Sec. III, which is self-contained. Conclusions and outlook can be found in Sec. IV.

II. METHOD

To explain our implementation of the CT-HYB in a concrete framework, we take a two-orbital model as an

example, that is,

$$H_{loc} = H_{\Delta} + H_V + H_{int} - \mu \sum_{a=1,2} \sum_{\sigma} n_{a\sigma}, \quad (1)$$

where $H_{\Delta} = \Delta \sum_{\sigma} (n_{1\sigma} - n_{2\sigma})$ represents the crystal field splitting and $H_V = V \sum_{\sigma} (c_{1\sigma}^{\dagger} c_{2\sigma} + h.c.)$ is the hybridization between two orbitals. For the interaction part, a general on-site form is considered,

$$H_{int} = \sum_{a=1,2} U n_{a\uparrow} n_{a\downarrow} + \sum_{\sigma} U' n_{1,\sigma} n_{2,\bar{\sigma}} + \sum_{\sigma} U'' n_{1\sigma} n_{2\sigma} - J(c_{1\downarrow}^{\dagger} c_{2\uparrow}^{\dagger} c_{2\downarrow} c_{1\uparrow} + c_{2\uparrow}^{\dagger} c_{2\downarrow}^{\dagger} c_{1\uparrow} c_{1\downarrow} + h.c.). \quad (2)$$

which contains the intraorbital and interorbital Coulomb interactions, as well as the spin-flip and pair-hopping processes.

As an impurity solver for the DMFT, CT-HYB employs the same idea as all the other CT-QMC impurity solvers; that is, it expands the impurity effective action around a certain limit and evaluates the expansion terms via stochastic sampling. Here, we only present the expressions relevant to this work. For a more detailed review of the CT-QMC methods, we suggest Ref. 13.

In the CT-HYB, the expansion of the “impurity + bath” action $S_{tot} = S_{loc} + S_{bath} + S_{hyb}$ around the atomic limit is carried out by integrating out the bath degrees of freedom. S_{loc} , S_{bath} are the actions for the local and the bath Hamiltonian, respectively. S_{hyb} is the hybridization between them,³ which is expanded order by order. The contraction of the bath operator b_{σ} , b_{σ}^{\dagger} follows Wick’s theorem, as the bath is noninteracting. This results in a determinant Det^{C_k} with the hybridization function $\Delta(\tau, \tau')$ as matrix elements. The full hybridization matrix usually can be decoupled into block diagonal form with respect to certain conserved quantum numbers, for example, the total particle number n , the spin σ_z and cluster momenta K . The final expression of the partition function can then be written as

$$\mathcal{Z} = \mathcal{Z}_b \mathcal{Z}_{loc} \prod_a \sum_{k_a} \int_0^{\beta} \prod_{i=1}^{k_a} d\tau_i d\tau'_i \text{Tr}(\mathcal{C}_{k_a}) Det^{C_{k_a}}. \quad (3)$$

Here, k_a is the expansion order (also the dimension of the determinant matrix) for the “a” flavor, where flavor represents spin, orbital, or cluster momenta. $\text{Tr}(\mathcal{C}_k) = \langle T_{\tau} \prod_a c_a(\tau'_1) c_a^{\dagger}(\tau_1) \cdots c_a(\tau'_k) c_a^{\dagger}(\tau_k) \rangle$ is the cluster trace of a group of “kinks”,¹² that is, cluster operators, in the interval $[0, \beta)$. From now on, we always work with the diagonal form of the hybridization function. The evaluation of $\text{Tr}(\mathcal{C}_{k_a})$ can be carried out in two ways. One can either express the c_{σ} , c_{σ}^{\dagger} operators as matrices in the eigenbasis of H_{loc} or employ the Krylov implementation¹⁴. The former one benefits from the diagonal form of the time evolution operators $e^{-H_{loc}\tau}$. The Krylov implementation, on the other hand, works in the particle-number basis, for which $e^{-H_{loc}\tau}$ becomes a sparse matrix. It uses the efficient Krylov-space method, which makes it possible to simulate up to typically seven orbital problems

at acceptable numerical costs. In this work, the first implementation is used, in which we diagonalize H_{loc} with respect to the conserved quantum numbers.¹⁵ The trace of the fermion operators is evaluated by first searching for nonzero overlap between different eigenstates with respect to the group of the cluster operators. The nonzero trace is, then, calculated along the trajectory found.

A. One-particle Green’s function

The impurity Green’s function is obtained by removing one row and column from the determinantal matrix. $G_a(i\omega_n)$ simply relates to $M = \Delta^{-1}$ by^{12,15}

$$G_{imp}(i\omega_n) = -\frac{1}{\beta} \sum_{i,j} M_{i,j} e^{i\omega_n(\tau_i - \tau_j)} \quad (4)$$

Alternatively, one can simulate the impurity Green’s function from the cluster trace at each Monte Carlo step;¹⁵ that is,

$$\begin{aligned} G_{imp}(i\omega_n) &= \frac{1}{\beta} \int_0^{\beta} e^{i\omega_n \tau} \langle c(\tau) c^{\dagger} \rangle d\tau \\ &= \frac{1}{\beta \mathcal{Z}} \int_0^{\beta} d\tau e^{i\omega_n \tau} \sum_{\phi} \langle \phi | e^{-\beta E_{\phi}} c(\tau) c^{\dagger} | \phi \rangle \end{aligned} \quad (5)$$

Here, $|\phi\rangle$ is the eigenstate of the Anderson impurity model, in terms of which the full partition function can be written as $\mathcal{Z} = \sum_{\phi} e^{-\beta E_{\phi}}$. For each specific configuration \mathcal{C}_k sampled in the CT-HYB, this expression has the following form:

$$\begin{aligned} G_{imp}^{C_k} &= \frac{\mathcal{Z}_{loc} \mathcal{Z}_b}{\beta \mathcal{Z}} \int_0^{\beta} d\tau e^{i\omega_n \tau} Det^{C_k} \\ &\quad \times \sum_m \langle m | e^{-\beta E_m} T_1^l c(\tau) T_{l+1}^k c^{\dagger} | m \rangle \end{aligned} \quad (6)$$

The explicit form of the determinant is given in Eqn. (3). T_1^l and T_{l+1}^k are the left and right lists of cluster operators $c(\tau)$, respectively, with the constraint $\tau_{l+1} < \tau < \tau_l$. The partition function corresponding to the configuration \mathcal{C}_k is given as

$$\begin{aligned} \mathcal{Z}_{C_k} &= \mathcal{Z}_{loc} \mathcal{Z}_b \sum_m \langle m | e^{-\beta E_m} T_1^l \times T_{l+1}^k | m \rangle Det^{C_k} \\ &= \mathcal{Z}_{loc} \mathcal{Z}_b \text{Tr}(\mathcal{C}_k) Det^{C_k}. \end{aligned} \quad (7)$$

By combining the above two equations, we have

$$\begin{aligned} G_{imp}^{C_k} &= \frac{\mathcal{Z}_{C_k}}{\mathcal{Z}} \frac{T}{\text{Tr}(\mathcal{C}_k)} \int_0^{\beta} d\tau e^{i\omega_n \tau} \\ &\quad \times \sum_{m,l} \langle m | e^{-\beta E_m} T_1^l c(\tau) T_{l+1}^k c^{\dagger} | m \rangle \\ &= \frac{\mathcal{Z}_{C_k}}{\mathcal{Z}} \frac{T}{\text{Tr}(\mathcal{C}_k)} \sum_{mn,pq,l} e^{-\beta E_m} T_{1,l}^{mn} c_{\omega}^{np} T_{l+1,k}^{pq} c^{\dagger,qm} \end{aligned} \quad (8)$$

with the notation $T_{1,l}^{m,n} \equiv \langle m|T_1^l|n \rangle$ and

$$c_\omega^{np} \equiv \frac{e^{(i\omega_n + E_n - E_p)\tau_l} - e^{(i\omega_n + E_n - E_p)\tau_{l+1}}}{i\omega_n + E_n - E_p} \langle n|c|p \rangle. \quad (9)$$

The ratio $\mathcal{Z}_{\mathcal{C}_k}/\mathcal{Z}$ is the probability of configuration \mathcal{C}_k being sampled in the Monte Carlo simulation.

When k_a is small, we measure G_{imp} directly from the cluster trace,¹⁵ that is, Eq. (8). Although this scheme is not very fast, it is more stable than Eq. (4). When k_a is large and Eq. (4) is used in the simulation, the high-frequency parts of G_{imp} converge much slower and contains more statistical errors than the low-frequency parts. As a result, the corresponding self-energy can be fluctuating at large ω_n . As already pointed out in the Introduction, the correct high-frequency behavior of $\Sigma_{imp}(i\omega_n)$ is crucial for the CT-HYB. Thus, special attention has to be paid to get rid of the noises in the self-energy data.

To the best of our knowledge, three schemes have been proposed for dealing with this problem. (1) Noise filtering. One can either smooth the noises at $\tau \approx \beta/2$ by averaging $G_{imp}(\tau)$ over a small range of τ (see Refs. 11 and 12) or apply the orthogonal polynomial filtering routine recently proposed by Boehnke *et al.*¹⁶ to achieve a smooth $G_{imp}(\tau)$ for all $\tau \in [0, \beta)$. By carefully choosing the order of the orthogonal polynomials, the impurity self-energy becomes smooth for all Matsubara frequencies. (2) Replacing the high-frequency tail of $\Sigma_{imp}(i\omega_n)$ with some well-behaving function. This function can be either the self-energy, calculated from a weak-coupling perturbation expansion, or the moment expansion of the Green's function.^{17,18} Such a replacement provides a smoothly behaving high-frequency tail of the self-energy function. However, the corresponding expression usually becomes complicated in the multi-orbital case and relies on the explicit form of the interaction term. (3) Measuring $G_{imp}(\tau)$ from higher order correlation functions.¹⁹ This method becomes advantageous for the density-density type interaction, for which the “segment picture”¹¹ can be used. For general type interactions, numerical cost has to be paid to calculate additional correlators.

Here, we propose a simple and stable scheme which does not rely on any direct noise filtering of $G_{imp}(\tau)$ and does not introduce any numerical cost to the CT-HYB simulations. This method does not depend on the explicit form of the interaction term and remains efficient in the multi-orbital calculations. The basic idea is to determine an approximate self-energy function by performing the perturbation expansion around the atomic limit, using the ‘dual-transformation’. As we will see later on, such a method generates systematic improvements to the atomic self-energy. The first-order expansion term already gives considerable corrections and reproduces the correct high-frequency behavior of $\Sigma_{imp}(i\omega_n)$.

The expansion around the atomic limit has been studied before.²⁰ In the strong-coupling region, this method yields results comparable to the numerical exact QMC

results. Here, we use an elegant and different way, that is, the “dual transformation”.²¹ This transformation has been used in the construction of the dual-fermion (DF) method, which gives an action well behaving in both the weak- and the strong-coupling limits. Thus, our perturbation expansion actually also works in the weak-coupling region.

The impurity model has the following action:

$$S[c^*, c] = S_{imp}[c^*, c] + \sum_n \sum_a c_a^* \Delta_a(i\omega_n) c_a \quad (10)$$

In the “dual transformation”, new variables f^*, f are introduced to rewrite the hybridization term in the following way:

$$e^{c_a^* \Delta_a(i\omega_n) c_a} \det\left[\frac{\Delta_a}{\alpha^2}\right]^{-1} = \int e^{-\alpha(c_a^* f_a + f_a^* c_a) - \frac{\alpha^2}{\Delta_a(i\omega_n)} f_a^* f_a} \mathcal{D}[f^*, f]. \quad (11)$$

The complex number α can be arbitrary in the above expression. In Ref. 21, it is taken as the impurity Green's function. This makes the correlator of the dual variables, that is, $G^d = -\langle f_a f_a^* \rangle$, behaves like the one-particle Green's function, which decreases as $1/i\omega_n$ for large ω_n . For simplicity, we take α as one. Although in this case, the dual variables can not be interpreted as fermions, the impurity Green's function remains the same.

Integrating out the c variable, the full action becomes a functional which only depends on variables f^*, f , that is,

$$\begin{aligned} \mathcal{Z} &= \mathcal{Z}_f \mathcal{Z}_b \int \mathcal{D}[f^*, f] e^{-\sum_a f_a^* \Delta_a^{-1} f_a} \\ &\int \mathcal{D}[c^*, c] e^{-S_{imp}[c^*, c]} \sum_{k_a} \frac{1}{k_a!} (c_a^* f_a + f_a^* c_a)^{k_a} \\ &= \mathcal{Z}_f \mathcal{Z}_b \int \mathcal{D}[f^*, f] e^{-\sum_a f_a^* G_a^{0,-1} f_a - V_d^{(4)} f_1 f_2^* f_3 f_4^*} \end{aligned} \quad (12)$$

where G_0^d is given as $[G_a^{at} - \Delta_a^{-1}]^{-1}$. The effective interaction of dual variables turns out to be the reducible four-point correlations of the atomic system, that is, $V_d^{(4)} = \chi_{12;34}^{at} - \delta_{1,2} \beta G_{12}^{at} G_{34}^{at} + \delta_{14} \beta G_{14}^{at} G_{23}^{at}$, with G^{at} being the atomic Green's function.

Since the dual transformation is mathematically exact, the two different actions which depend on only c variables [i.e., Eq. (10)] and f variables [i.e., Eq. (12)] are equivalent. Thus, we can obtain an exact relation between the correlators G_a and G_a^d from differentiating the two actions with respect to Δ_a . This yields:

$$G_a = -\Delta_a^{-1} - \Delta_a^{-1} G_a^d \Delta_a^{-1}, \quad (13)$$

where G_a^d is obtained from the Dyson equation, that is, $G_a^d = [G_0^d - \Sigma_a^d]^{-1}$. Σ_a^d is the self-energy function of the dual variables. The expression of $\chi_{12;34}^{imp}$ can be found in the literature, (e.g., Refs. 22–24). If the interaction of the

dual variables in Eq. (12) is neglected, the atomic self-energy will be recovered. This can be seen by inserting G_0^d into Eq. (13). We have

$$G_a(i\omega_n) = G_a^{at}/(1 - \Delta_a G_a^{at}). \quad (14)$$

Then, from the Dyson equation, we immediately see that

$$\begin{aligned} \Sigma_a^{imp} &= i\omega_n + \mu - \Delta_a - G_a^{-1}(i\omega_n) \\ &= i\omega_n + \mu - 1/G_a^{at} = \Sigma_a^{at} \end{aligned} \quad (15)$$

Thus, one can imagine the interaction term in Eq. (12) will generate systematic corrections to the atomic self-energy.

By including the interaction and further restricting the calculation of Σ_a^d to the first order, we have

$$\Sigma_{a,\sigma}^d(i\omega_n) = -\frac{1}{\beta} \sum_b \sum_{\omega'_n} V_{aa;bb}^{d,(4)}(i\omega_n; i\omega'_n) G_b^d(i\omega'_n) \quad (16)$$

In this equation, only the element $V_{12;34}^{d,(4)}\delta_{12}\delta_{34}$ is required. Additionally, this calculation can be further accelerated by employing the look-up routine and the symmetry of $\chi_{12;34}^{at}$, which is shown in Sec. II B. By doing so, the perturbation expansion remains very efficient in multi-orbital calculations.

As a benchmark, we first apply the dual expansion scheme by restudying the Bethe lattice with different bandwidths, that is, $W_2 = 2W_1$, where the orbital-selective Mott transition can happen.^{11,25–35} We directly solved the DMFT equation with the high-frequency supplemented self-energy function, instead of using Eq. (20) in Ref. 12. Our self-energy data in Fig. 1 is identical to

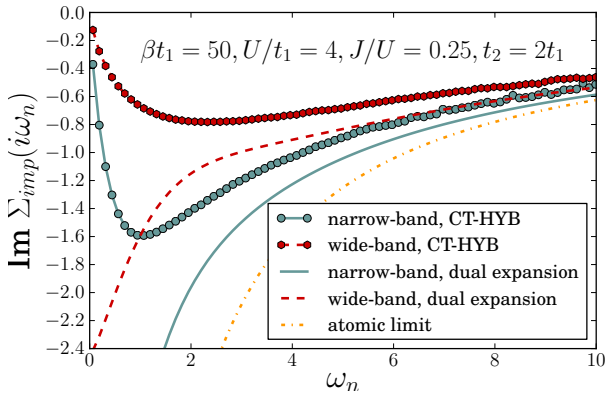


FIG. 1. Benchmark: imaginary part of the impurity self-energies for $\beta t_1 = 50, U/t_1 = 4, J/U = 0.25$ in unit of t_1 . Both the narrow and the wide bands are metallic. The dual expansion gives two different asymptotic behaviors of the self-energy for two different bands, as expected. However, the atomic self-energy does not have such a resolution.

those in Fig. 12 of Ref. 12, meaning that the dual expansion method is reliable to produce the high-frequency tail of the self-energy and can be used in the CT-HYB

for solving impurity problems. To see the performance of the dual expansion method for a finite spatial-dimension problem, in Fig. 2 we show the comparison of the self-energy function calculated for a two-orbital Hubbard model in two dimension [see the Hamiltonian in Eq. (1)]. The improvement from the dual expansion is clearly seen from the agreement between the CT-HYB and the dual expansion results. Increasing the hybridization strength, this agreement becomes even better. Thus, a smaller number of Matsubara frequencies is required to simulate in such a case. However, the atomic self-energy has a larger deviation from the CT-HYB results for smaller ω_n . Similar ideas were used to formulate effective impurity solvers^{22,24} for the DMFT. We use it here to get the correct high-frequency tail of the impurity self-energy, while still keeping the low-frequency self-energy function simulated from the QMC. This method only needs the hybridization function at each DMFT iteration. The dual-expansion can be carried out independently of the CT-HYB simulation. Thus, it does not introduce additional numerical cost to the CT-HYB, which is another essential difference with respect to previous works.^{15–19}

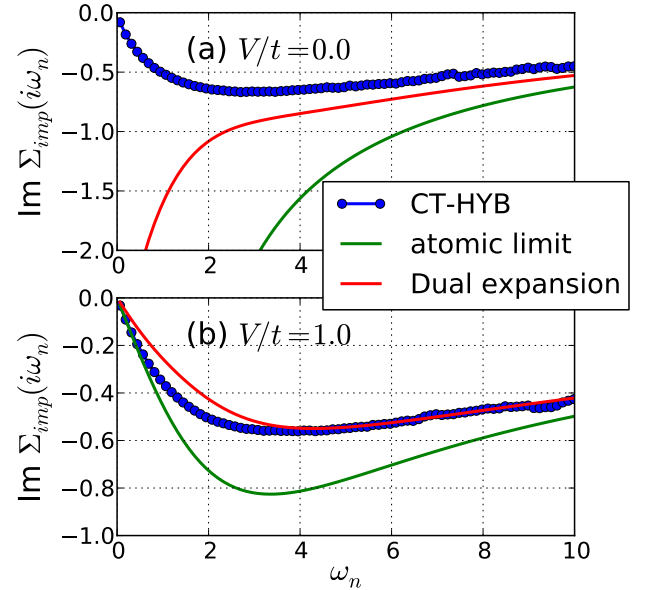


FIG. 2. The comparison of the impurity self-energy calculated from the CT-HYB, atomic Hubbard model and the dual expansion method. The parameter sets for the two-orbital Hubbard model are $\beta t = 50, U/t = 4.0, J/U = 0.25, V/t = 1.0$. See the text for more details.

B. Four-point correlation function $\chi_{12;34}$

The dual expansion, discussed in the above section, requires the knowledge of the atomic four-point correlation function $\chi_{12;34}^{at}$. In the multi-orbital case, such a

calculation can be hard since the large-dimensional matrix multiplication is time consuming. In this case, one can again use the block diagonal form of the Hamiltonian matrix and employ the look-up routine as we did in the trace calculation. Here, we want to further simplify the calculation by employing the symmetry of $\chi_{12;34}^{at}$. Such a symmetry turns out to be also very useful in the simulation of the impurity four-point correlation function $\chi_{12;34}^{imp}$. Thus, in this section we try to keep our discussion general. We start from the simulation of the $\chi_{12;34}^{imp}$ in the CT-HYB and discuss the symmetries of it afterward. The same symmetry requirements are satisfied by $\chi_{12;34}^{at}$ as well.

Although in the CT-HYB, Wick's theorem apparently is not supported by the impurity action, the four-point correlation function can be simulated by removing two rows and two columns from the determinant matrix, which results in an expression analogous to those for the CT-INT and the CT-AUX. Effectively, one can still simulate the four-point correlation function as if Wick's theorem holds. Here, we use the following notation to symbolically represent this expression:

$$\begin{aligned}\chi_{12;34} &:= \langle c_1 c_2^* c_3 c_4^* \rangle \\ &= \frac{\langle c_1 c_2^* \rangle \langle c_3 c_4^* \rangle - \langle c_1 c_4^* \rangle \langle c_2 c_3^* \rangle}{g_{12}(\omega_1, \omega_2) g_{34}(\omega_3, \omega_4) - g_{14}(\omega_1, \omega_4) g_{32}(\omega_3, \omega_2)}\end{aligned}\quad (17)$$

where labels 12; 34 represent “orbitals, sites, spins,” etc. In the CT-HYB, the two-frequency dependent propagators $g_{\alpha\beta}(\omega, \omega')$ is given as

$$g_{\alpha\beta}(\omega_1, \omega_2) = -\frac{1}{\beta} \sum_{i,j} e^{i\omega_1 \tau_i} M_{ij}^{\alpha\beta} e^{-i\omega_2 \tau_j}. \quad (18)$$

It has the following symmetry in Matsubara frequency space:

$$g_{\alpha\beta}(\omega_1, \omega_2) = g_{\alpha\beta}^*(-\omega_1, -\omega_2), \quad (19)$$

which reduces the numerical effort by a factor of two. A similar symmetry is also satisfied by χ :

$$\chi_{12;34} = \chi_{12;34}^{\Omega}(\omega, \omega') = \chi_{12;34}^{-\Omega,*}(-\omega, -\omega'). \quad (20)$$

In what follows, we denote $\omega = \omega_1$, $\omega + \Omega = \omega_2$, $\omega' + \Omega = \omega_3$, $\omega' = \omega_4$. Equation (20) says, only for $\Omega > 0$, χ needs to be simulated.

Symmetry (20) relates the positive frequencies to the corresponding negative frequencies of χ . It is also possible to find symmetries which connect different ω , ω' in the same Ω sector. This can be achieved via the fact that $\chi_{12;34}$ is antisymmetric under the exchange $1 \Leftrightarrow 3$ and $2 \Leftrightarrow 4$:

$$\chi_{34;12}(\omega' + \Omega, \omega + \Omega; -\Omega) = \chi_{12;34}(\omega, \omega'; \Omega). \quad (21)$$

Combining Eq. (21) with Eq. (20), we have

$$\chi_{34;12}(-\omega' - \Omega, -\omega - \Omega; \Omega) = \chi_{12;34}^*(\omega, \omega'; \Omega). \quad (22)$$

Given the spin configurations of different χ channels, we find $\chi_{12;34}^{\sigma\sigma;\sigma\sigma}$ satisfies both symmetries in Eqs. (20) and (22). However, $\chi_{12;34}^{\sigma\sigma;\bar{\sigma}\bar{\sigma}}$ only satisfies the symmetry shown in Eq. (20) and the following relation:

$$\chi_{12;34}^{\sigma\sigma;\bar{\sigma}\bar{\sigma}} = \chi_{34;12}^{\bar{\sigma}\bar{\sigma};\sigma\sigma}. \quad (23)$$

One can implement the symmetries in Eqs. (20) and (22) as follows. (1) $\chi^{\uparrow\uparrow;\uparrow\uparrow}$, $\chi^{\downarrow\downarrow;\downarrow\downarrow}$, and $\chi^{\uparrow\downarrow;\downarrow\uparrow}$ are simulated only for $\Omega > 0$. (2) For each specific Ω considered, Eq. (22) is further applied to $\chi^{\uparrow\downarrow;\uparrow\uparrow}$ and $\chi^{\downarrow\downarrow;\downarrow\downarrow}$. Only for parts of the frequency points in this Ω -sector do $\chi^{\uparrow\downarrow;\uparrow\uparrow}$ and $\chi^{\downarrow\downarrow;\downarrow\downarrow}$ need to be simulated. (3) At the end of the calculation, $\Omega < 0$ components are calculated through Eq. (21). (4) $\chi^{\downarrow\downarrow;\uparrow\uparrow}$ is calculated by Eq. (23). In addition to the symmetries shown in Eqs. (20) and (22), it is possible to find more symmetries to relate different frequency sectors.

Before finishing this section, we want to note that the four-point correlation function is useful not only for the physical response function and the dual-expansion scheme, but also relates closely with the extension of the DMFT. In the DF method²¹ and the dynamical vertex approximation (DFA),²³ the nonlocal self-energy is constructed from the impurity two-particle vertices.

III. APPLICATION

As a typical application, we consider here a two-orbital Hubbard model [see the Hamiltonian in Eq. (1)], with rotationally invariant interactions, i.e. $U' = U - 2J$, $U'' = U' - J$. To make a link with realistic material systems, this multiorbital Hubbard model can be viewed as an effective model for the e_g -orbital systems. The rotational invariance of the interaction term is not obligatory in the CT-HYB solver; here, we use it only as one possible situation. By making use of the DMFT, the two-orbital Hubbard model has been studied by many groups.^{12,36-43} These calculations are either based on a semicircular density of states, which corresponds to the Bethe lattice, or they employ an impurity solver with certain limitations in temperature or interaction strength. Here, we solve the DMFT equation at finite dimension and temperatures. In these cases, the DMFT loop cannot be closed by a simple relation in the imaginary-time space like on the Bethe lattice. Thus, our dual-expansion method discussed in Sec. II A turns to be a decisive tool. Our calculations are mainly performed on ordinary desktop computers.

Compared to the single-orbital case, two issues in a multiorbital model are of obvious interests:

(1) *What is the effect of the orbital fluctuations?* The general believe is, that it is competitive to the Coulomb interaction. As a result, the metallic state can be stabilized up to a large interaction value^{31,44}.

(2) *How does the Hund's coupling modify the transition from the metal to Mott insulator (MIT)?* It is known

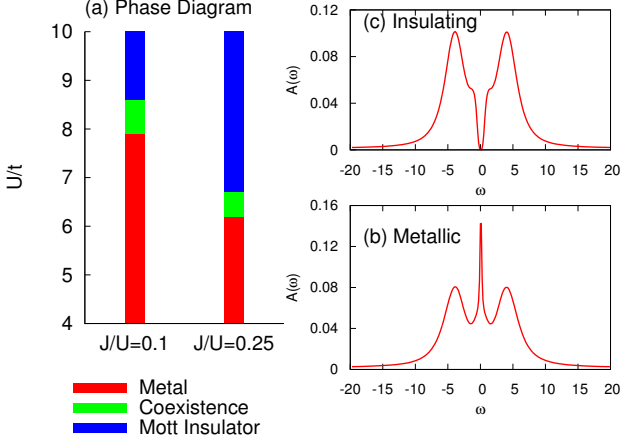


FIG. 3. The phase diagram of the two-orbital Hubbard model at half filling. The MIT at $\beta t = 50$ for two values of J/U are shown as histograms. The two local density of states on the right-hand side correspond to the two solutions for $U/t = 8.4$, $J/U = 0.1$.

that the two-orbital Hubbard model behaves quite differently with and without J .^{36,37}

The phase diagrams of the two-orbital Hubbard model can be found in Refs. 37 and 42. Here we study, in particular, the coexistence region for different values of J in Fig. 3 (a), which indicates the MIT is of first order. Compared to the phase diagrams for the Bethe lattice,^{37,42} the reduction of the spatial dimension does not change significantly the critical Coulomb interaction value of U_c when it is normalized by the full bandwidth. However, U_c becomes larger compared to the single-orbital model, which confirms that the orbital fluctuation stabilize the metallic phase. With the increase of the Hund's rule coupling J , we found the coexistence region to become smaller. For the two values of J/U in our calculations, the reduction is about 0.2 eV. On the other hand, Bulla *et al.*⁴⁵ found, for $J/U > 0.25$, the transition to be of second order. At $J/U = 0.25$, our results show that the coexistence region still has a reasonably large width. Thus, we believe that even for $J/U > 0.25$, the MIT remains first order. Whether, the coexistence region completely disappears with the further increase of J/U deserves more investigations.

On the right-hand side of Fig. 3, two different solutions of the local density of state, that is, $A(\omega)$, are displayed for $U/t = 8.4$. They correspond to the metallic, see Fig. 3 (b), and insulating states [see Fig. 3 (c)] in the coexistence region. $A(\omega)$ is obtained by using the stochastic analytical continuation directly on the Matsubara data of $G_{imp}(i\omega_n)$.⁴⁶

In Fig. 4, the typical behavior of the metal-to-band-insulator transition is shown by calculating the impurity Green's function and the corresponding self-energy as a function of the hybridization. Increasing the hybridization V/t tends to open a band gap. Furthermore, with the increase of V/t , the impurity Green's function

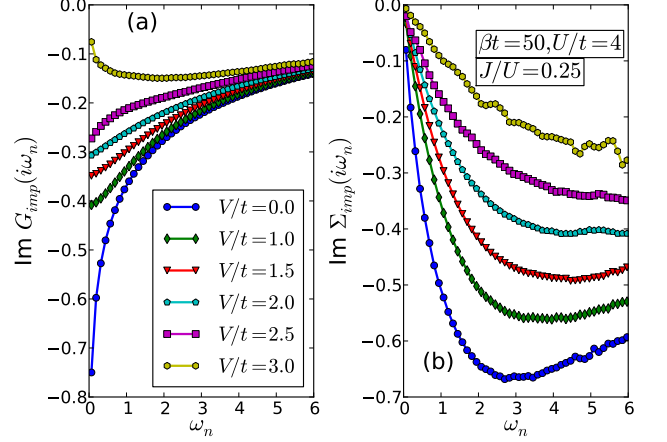


FIG. 4. Behavior of the impurity self-energy and Green's function around the metal-to-band-insulator transition as functions of the hybridization strength V/t .

at the lowest Matsubara frequency becomes smaller and finally approaches zero [see Fig. 4 (a)]. The metal-to-band-insulator transition happens somewhere between $V/t = 2.5$ and 3.0 for $U/t = 4$. This transition is not visible from the self-energy plot, where $\Sigma_{imp}(i\omega_n)$ behaves similarly for different values of V/t . The slope, that is, $\partial \Sigma_{imp}(\omega)/\partial \omega|_{\omega_0}$, remains negative for all hybridization strengths [see Fig. 4 (b)]. In contrast, the slope of the local Green's function around ω_0 has different signs before and after the metal-insulator (band) transition.

Increasing further the value of U/t strengthens both the intra- and interorbital interactions. Finally, for val-

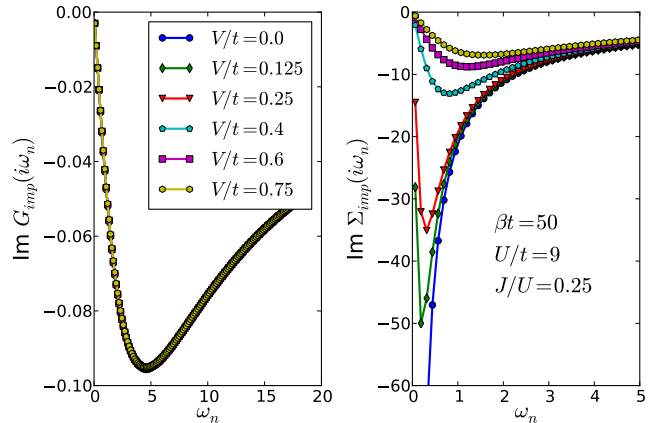


FIG. 5. Similar to Fig. 4, but with different interaction strength $U/t = 9$, where a Mott-insulating state is found at $\Delta/t = 0, 0.125, 0.25$. The increase of the hybridization between two orbitals greatly changes the behavior of the self-energy, while it leaves the one-particle Green's function essentially unchanged.

ues of U/t of the order of the noninteracting bandwidth, the metal to band-insulator transition is replaced by the Mott-insulator-to-band-insulator crossover as a function of the hybridization strength Δ/t . This behavior is displayed in Fig. 5. In contrast to the metal to band-insulator transition shown in Fig. 4, in Fig. 5 (with a choice of $U/t = 9$), the local Green's function stays nearly unchanged under modifying the hybridization strength V/t , that is, G_{imp} shows an insulating behavior for all values of V/t . However, for different values of V/t , the insulating nature is indeed different. This can be seen from the variation of the self-energy function shown in the right-hand side of Fig. 5. Increasing V/t , results in increasing of $\partial\Sigma(\omega)/\partial\omega|_{\omega_0}$ for any finite V/t , indicating the crossover from Mott-insulator to band-insulator behavior.⁴⁷

By applying the symmetries presented in Sec. II B, we show the results for the interorbital and intraorbital reducible spin susceptibilities in Fig. 6 for $\beta t = 20$, $U/t = 6$, $J/U = 0.25$, and $V/t = 0$, with a, b the orbital indices:

$$\tilde{\chi}_{\Omega}^{spin,ab}(\omega_n, \omega'_n) = \frac{1}{2}(\tilde{\chi}_{ab,\Omega}^{\sigma\sigma,\sigma\sigma} - \tilde{\chi}_{ab,\Omega}^{\sigma\sigma,\bar{\sigma}\bar{\sigma}}) \quad (24)$$

$\tilde{\chi}_{\Omega}^{spin,ab}(\omega_n, \omega'_n)$ are the impurity susceptibilities with the subtraction of the impurity bubble susceptibilities. They are plotted as functions of the two fermionic frequencies ω_n, ω'_n for fixed $\Omega = 0$. While here only the $\Omega = 0$ component is given, the implementation discussed in Sec. II B works for any value of Ω . Figures 6(a) and 6(b) refer to the three-dimensional (3D) plots of $\tilde{\chi}_{\Omega}^{spin,ab}(\omega_n, \omega'_n)$; the corresponding 2D top-view plots are shown in Figs. 6(c) and 6(d). Based on the CT-HYB, the four-point correlation functions were recently also calculated for the effective one and four-orbital systems^{16,48} for different problems. Another efficient and stable, but approximate, algorithm can be found in Ref. 49.

From Fig. 6, we see that the reducible two-particle susceptibility $\tilde{\chi}_{\Omega=0}^{spin,ab}(\omega_n, \omega'_n)$ decays rather fast as a function of ω_n and ω'_n . The dominant contribution comes from the elements with $\omega_n = 0$, or $\omega'_n = 0$, or $\omega_n = \omega'_n$. For our parameter set, the interorbital spin susceptibility shows a sharper structure than the intraorbital one, which can be viewed as a precursor of the possible orbital antiferromagnetic order.

IV. CONCLUSION

In this paper, we showed how the high-frequency tail of the self-energy can be calculated in a controlled manner from the dual transformation in CT-HYB. This scheme provides an efficient recipe for finite-dimension DMFT studies when taking the CT-HYB as an impurity solver. Our procedure is based on a Matsubara frequency space simulation and produces more moments from the dual expansion. Thus, it generates an improved high-frequency self-energy behavior. Most importantly, it does not intro-

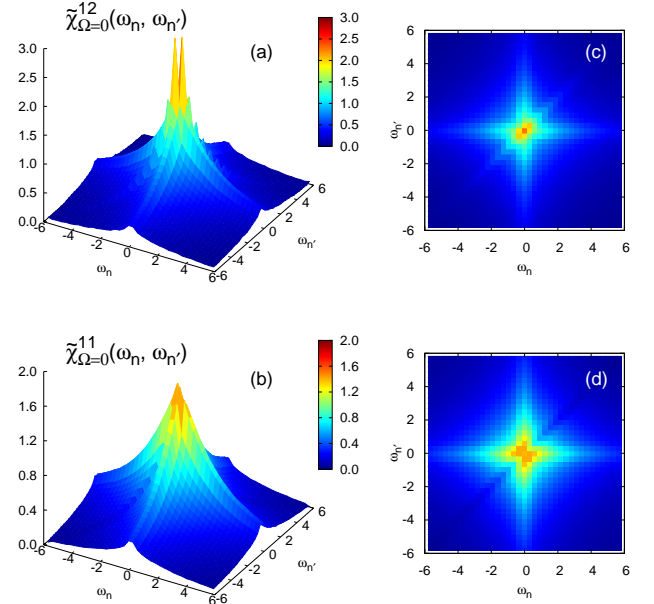


FIG. 6. The interorbital, that is, $\tilde{\chi}_{\Omega=0}^{12}$, and intraorbital, that is, $\tilde{\chi}_{\Omega=0}^{11}$, components of the reducible impurity two-particle susceptibility for $\beta t = 20$, $U/t = 6$, $J/U = 0.25$.

duce any additional numerical cost to the runtime simulation. We also simulated the four-point correlation function for different spin configurations in the particle-hole channel. To this end, we implemented different symmetries to reduce the memory and CPU requirements without losing accuracy.

As a first application, we demonstrated the usefulness of our method for a two-orbital model with a general on-site interaction. From this study, we deduced a substantial influence of the Hund's rule coupling on the metal-insulator transition phase diagram, especially on the co-existence region. In particular, we find that for any finite value of J/t , the MIT stays first order.

Our scheme is also of particular use for connecting the DF method, which many be viewed as a nonlocal extension of the DMFT, with *a priori* DFT techniques. A multiorbital DF calculation will be especially interesting and rewarding for the DFT + DF study of material systems. In such study, the CT-HYB effectively works on an impurity problem with the DFT dispersions as input. Thus, one has a good control on the "minus-sign" problem. The high-momentum resolution, provided by the DF algorithm, makes the result ready to be compared with experiments, such as ARPES data.

ACKNOWLEDGMENTS

One of us (G. Li) acknowledges the valuable discussions with Philipp Werner, Hartmut Monien, Xi Dai and Zhong Fang and is grateful for the hospitality of Institute of Physics, Chinese Academy of Science. We thank

Fakher Assaad for providing us the initial stochastic analytical continuation code, from which the extension to Matsubara frequency space was made. This work was supported by the DFG Grants No. Ha 1537/23-1 within the Forschergruppe FOR 1162.

-
- * gangli@physik.uni-wuerzburg.de
- ¹ E. Müller-Hartmann, *Zeitschrift für Physik B Condensed Matter* **74**, 507 (1989), 10.1007/BF01311397.
 - ² W. Metzner and D. Vollhardt, *Phys. Rev. Lett.* **62**, 324 (1989).
 - ³ A. Georges, G. Kotliar, W. Krauth, and M. J. Rozenberg, *Rev. Mod. Phys.* **68**, 13 (1996).
 - ⁴ M. Caffarel and W. Krauth, *Phys. Rev. Lett.* **72**, 1545 (1994).
 - ⁵ A. Georges and G. Kotliar, *Phys. Rev. B* **45**, 6479 (1992).
 - ⁶ H. Keiter and J. C. Kimball, *Phys. Rev. Lett.* **25**, 672 (1970).
 - ⁷ N. E. Bickers, D. L. Cox, and J. W. Wilkins, *Phys. Rev. B* **36**, 2036 (1987).
 - ⁸ R. Bulla, *Adv. Sol. State Phys.* **46**, 169 (2000).
 - ⁹ A. N. Rubtsov, V. V. Savkin, and A. I. Lichtenstein, *Phys. Rev. B* **72**, 035122 (2005).
 - ¹⁰ P. E. Gull, P. Werner and M. Troyer, *EPL* **82**, 57003 (2008).
 - ¹¹ P. Werner, A. Comanac, L. de' Medici, M. Troyer, and A. J. Millis, *Phys. Rev. Lett.* **97**, 076405 (2006).
 - ¹² P. Werner and A. J. Millis, *Phys. Rev. B* **74**, 155107 (2006).
 - ¹³ E. Gull, A. J. Millis, A. I. Lichtenstein, A. N. Rubtsov, M. Troyer, and P. Werner, *Rev. Mod. Phys.* **83**, 349 (2011).
 - ¹⁴ A. M. Läuchli and P. Werner, *Phys. Rev. B* **80**, 235117 (2009).
 - ¹⁵ K. Haule, *Phys. Rev. B* **75**, 155113 (2007).
 - ¹⁶ L. Boehnke, H. Hafermann, M. Ferrero, F. Lechermann, and O. Parcollet, *Phys. Rev. B* **84**, 075145 (2011).
 - ¹⁷ E. Gull, *Continuous-time quantum Monte Carlo algorithms for fermions* (Ph.D. thesis, 2008).
 - ¹⁸ X. Wang, H. T. Dang, and A. J. Millis, *Phys. Rev. B* **84**, 073104 (2011).
 - ¹⁹ H. Hafermann, K. R. Patton, and P. Werner, *ArXiv e-prints* (2011), [arXiv:1108.1936 \[cond-mat.str-el\]](https://arxiv.org/abs/1108.1936).
 - ²⁰ X. Dai, K. Haule, and G. Kotliar, *Phys. Rev. B* **72**, 045111 (2005).
 - ²¹ A. N. Rubtsov, M. I. Katsnelson, A. I. Lichtenstein, and A. Georges, *Phys. Rev. B* **79**, 045133 (2009).
 - ²² I. Krivenko, A. Rubtsov, M. Katsnelson, and A. Lichtenstein, *JETP Letters* **91**, 319 (2010).
 - ²³ A. Toschi, A. A. Katanin, and K. Held, *Phys. Rev. B* **75**, 045118 (2007).
 - ²⁴ H. Hafermann, C. Jung, S. Brener, M. I. Katsnelson, A. N. Rubtsov, and A. I. Lichtenstein, *EPL (Europhysics Letters)* **85**, 27007 (2009).
 - ²⁵ V. I. Anisimov, I. A. Nekrasov, D. E. Kondakov, T. M. Rice, and M. Sigríst, *Eur. Phys. J. B* **25**, 191 (2002).
 - ²⁶ A. Koga, N. Kawakami, T. M. Rice, and M. Sigríst, *Phys. Rev. Lett.* **92**, 216402 (2004).
 - ²⁷ S. Biermann, L. de' Medici, and A. Georges, *Phys. Rev. Lett.* **95**, 206401 (2005).
 - ²⁸ L. de' Medici, A. Georges, and S. Biermann, *Phys. Rev. B* **72**, 205124 (2005).
 - ²⁹ T. A. Costi and A. Liebsch, *Phys. Rev. Lett.* **99**, 236404 (2007).
 - ³⁰ A. Liebsch, *Phys. Rev. Lett.* **95**, 116402 (2005).
 - ³¹ K. Inaba, A. Koga, S.-i. Suga, and N. Kawakami, *Phys. Rev. B* **72**, 085112 (2005).
 - ³² A. Liebsch, *Phys. Rev. Lett.* **91**, 226401 (2003).
 - ³³ J. Bünenmann, D. Rasch, and F. Gebhard, *Journal of Physics: Condensed Matter* **19**, 436206 (2007).
 - ³⁴ K. Inaba and A. Koga, *Phys. Rev. B* **73**, 155106 (2006).
 - ³⁵ C. Knecht, N. Blümer, and P. G. J. van Dongen, *Phys. Rev. B* **72**, 081103 (2005).
 - ³⁶ F. Lu, W.-H. Wang, and L.-J. Zou, *Phys. Rev. B* **77**, 125117 (2008).
 - ³⁷ P. Werner and A. J. Millis, *Phys. Rev. Lett.* **99**, 126405 (2007).
 - ³⁸ M. Sentef, J. Kuneš, P. Werner, and A. P. Kampf, *Phys. Rev. B* **80**, 155116 (2009).
 - ³⁹ R. Peters, N. Kawakami, and T. Pruschke, *Phys. Rev. B* **83**, 125110 (2011).
 - ⁴⁰ K. Inaba and A. Koga, *Journal of the Physical Society of Japan* **76**, 094712 (2007).
 - ⁴¹ Y. Koyama, A. Koga, N. Kawakami, and P. Werner, *Physica B: Condensed Matter* **404**, 3267 (2009), proceedings of the International Conference on Strongly Correlated Electron Systems.
 - ⁴² L. de' Medici, *Phys. Rev. B* **83**, 205112 (2011).
 - ⁴³ L. de' Medici, J. Mravlje, and A. Georges, *Phys. Rev. Lett.* **107**, 256401 (2011).
 - ⁴⁴ A. Koga, Y. Imai, and N. Kawakami, *Phys. Rev. B* **66**, 165107 (2002).
 - ⁴⁵ T. Pruschke and R. Bulla, *The European Physical Journal B - Condensed Matter and Complex Systems* **44**, 217 (2005), 10.1140/epjb/e2005-00117-4.
 - ⁴⁶ K. S. D. Beach, *ArXiv Condensed Matter e-prints* (2004), [arXiv:cond-mat/0403055](https://arxiv.org/abs/cond-mat/0403055).
 - ⁴⁷ A. Fuhrmann, D. Heilmann, and H. Monien, *Phys. Rev. B* **73**, 245118 (2006).
 - ⁴⁸ H. Park, K. Haule, and G. Kotliar, *Phys. Rev. Lett.* **107**, 137007 (2011).
 - ⁴⁹ J. Kuneš, *Phys. Rev. B* **83**, 085102 (2011).